



Engineering catalyst supports to stabilize PdO_x two-dimensional rafts for water-tolerant methane oxidation

Haifeng Xiong^{®1,12}, Deepak Kunwar^{2,12}, Dong Jiang^{®3,12}, Carlos E. García-Vargas^{®3}, Hengyu Li¹, Congcong Du¹, Griffin Canning², Xavier Isidro Pereira-Hernandez^{®3}, Qiang Wan⁴, Sen Lin^{®4}, Stephen C. Purdy^{®5}, Jeffrey T. Miller⁵, Kevin Leung⁶, Stanley S. Chou^{®6}, Hidde H. Brongersma⁷, Rik ter Veen^{®8}, Jianyu Huang⁹, Hua Guo^{®10}, Yong Wang^{3,11} and Abhaya K. Datye^{®2}

The treatment of emissions from natural gas engines is an important area of research since methane is a potent greenhouse gas. The benchmark catalysts, based on Pd, still face challenges such as water poisoning and long-term stability. Here we report an approach for catalyst synthesis that relies on the trapping of metal single atoms on the support surface, in thermally stable form, to modify the nature of further deposited metal/metal oxide. By anchoring Pt ions on a catalyst support we can tailor the morphology of the deposited phase. In particular, two-dimensional (2D) rafts of PdO_x are formed, resulting in higher reaction rates and improved water tolerance during methane oxidation. The results show that modifying the support by trapping single atoms could provide an important addition to the toolkit of catalyst designers for controlling the nucleation and growth of metal and metal oxide clusters in heterogeneous catalysts.

he control over the size, morphology and oxidation state of clusters and nanoparticles is important for achieving optimum performance in heterogeneous catalysis. There are limited means available for catalyst designers to influence the nature of the active phase, especially when the catalysts are subjected to elevated temperatures. The widely used approaches for industrial catalysts involve adsorption of the metal salt precursor on an oxide support¹, via the methods of deposition-precipitation or strong electrostatic adsorption (SEA)2. Using these approaches, it is possible to achieve atomic dispersion of the deposited metal on a number of catalyst supports³⁻⁷. The interaction between the metal salt precursor and the functional groups on the surface (for example, hydroxyls) determines the surface concentration of the dispersed phase. The nature and morphology of the dispersed phase depend on the surface structure of the oxide support^{8,9}, which can be manipulated by using faceted oxides as supports, or by introducing ligands on the support¹⁰. By precalcining the support, the number of hydroxyls on the support can be changed, which allows some control over the metal deposition. However, once the catalyst is treated at high temperatures (>300 °C), the mobility of the deposited metal leads to formation of thermodynamically stable structures, where the influence of the initial preparation steps is lost. Therefore, alternative approaches must be explored to generate a catalyst suitable for high temperature applications such as methane oxidation.

Methane combustion catalysis is becoming increasingly important to address the emission of unburned methane associated with the widespread use of natural gas as a clean fuel for vehicles and for power generation. Pd-based catalysts show the highest activity for methane oxidation. However, they suffer from insufficient low-temperature performance, rapid deactivation due to the presence of H₂O and sintering of the Pd phase^{11,12}. Because of the excess O₂ present in the reactant stream, the stable phase of Pd under reaction is PdO. The sintering of Pd catalysts under steam is ascribed to the formation and migration of mobile Pd-OH entities in the presence of H₂O molecules¹³, which are strongly adsorbed on the PdO surface. The binding of H₂O to the PdO also causes poisoning of the surface sites for methane oxidation^{14,15}. Such surface poisoning by steam is confirmed by the fact that the surface coverage of CH₄ in the presence of water vapour is limited to only 3% of the saturation coverage of a pure CH₄ layer on PdO (101)¹⁶. In our previous work, when Pd catalysts were reduced before reaction, we observed enhanced low-temperature reactivity¹⁷. Similar enhanced reactivity due to prereduction of Pd catalysts (also termed in situ activation) has been reported by other workers^{18,19}. We attribute this higher reactivity to a different form of surface Pd oxide formed on the surface of the reduced Pd catalyst (in contrast to bulk PdO). This is consistent with density functional theory (DFT) calculations, which show that a surface oxide is more active than bulk PdO nanoparticles^{20,21}. However, when Pd-based catalysts are used for methane

¹State Key Laboratory of Physical Chemistry of Solid Surfaces, College of Chemistry and Chemical Engineering, Xiamen University, Xiamen, China.

²Department of Chemical and Biological Engineering and Center for Micro-Engineered Materials, University of New Mexico, Albuquerque, NM, USA.

³The Gene & Linda Voiland School of Chemical Engineering and Bioengineering, Washington State University, Pullman, WA, USA.

⁴State Key Laboratory of Photocatalysis on Energy and Environment, College of Chemistry, Fuzhou University, Fuzhou, China.

⁵Davidson School of Chemical Engineering, Purdue University, West Lafayette, IN, USA.

⁶Sandia National Laboratories, Albuquerque, NM, USA.

⁷ION-TOF GmbH, Münster, Germany.

⁸Tascon GmbH, Münster, Germany.

⁹Clean Nano Energy Center, State Key Laboratory of Metastable Materials Science and Technology, Yanshan University, Qinhuangdao, China.

¹⁰Department of Chemistry and Chemical Biology, University of New Mexico, Albuquerque, NM, USA.

¹¹Institute for Integrated Catalysis, Pacific Northwest National Laboratory, Richland, WA, USA.

¹²These authors contributed equally: Haifeng Xiong, Deepak Kunwar, Dong Jiang.

⁸⁰e-mail: haifengxiong@xmu.edu.cn; hguo@unm.edu; yong.wang@pnnl.gov; datye@unm.edu

combustion, the metal Pd nanoparticle transforms to PdO, leading to decreased catalytic activity 22 . A well-known approach for improving the stability and reactivity of Pd-based catalysts is to add Pt, which stabilizes the Pd phase in a metallic state by forming bimetallic PtPd even under oxidizing conditions, leading to enhanced resistance to adsorption of water molecules. However, the bimetallic Pt–Pd catalysts are not as resistant to sintering as PdO catalysts, showing the formation of large alloy Pt–Pd particles (>20 nm) and declined catalytic reactivity 17,23 . Therefore, there is an urgent need to develop strategies of forming an active Pd phase that is resistant to $\rm H_2O$ poisoning and to catalyst sintering 24 .

In this work, we have modified the catalyst support via strongly bound Pt single atoms (atom trapping^{25–27}, high temperature vapour phase synthesis), to control the nature of the metal and metal oxide phase. The trapped Pt atoms on the ceria support therefore modify the nucleation and morphology of the secondary dispersed phase. We show that a 2D morphology of the PdO_x phase synthesized with this approach is thermally stable and resistant to water poisoning, showing increased reactivity in methane oxidation. The catalysts prepared thus overcome the disadvantages of large PdO particles that are readily poisoned by water, leading to decreased activity, or single atom Pd on the support that is less active for methane oxidation²⁸. The light-off methane oxidation in this work was carried out up to 650 °C and the steady state reaction was performed at 500 °C, which is preferred in exhaust catalysis to meet future emission regulations, especially for natural gas vehicles (NGVs) where the exhaust temperature is typically below 500-550 °C (ref. 29).

Results

Engineering of the catalyst support via atom trapping. In this work, we first modified the ceria with atomically dispersed Pt to prepare the catalyst support (Fig. 1a). This involves deposition of a Pt precursor (1 wt.% Pt) on the ceria support, then heating to 800 °C in air for 10 h. Since the Pt is present in an atomically dispersed form, we will refer to this support as 1Pt@CeO₂ (Fig. 1b). Next, we deposited additional 2 wt.% Pt on this engineered ceria support. We found that the added Pt does not form atomically dispersed species as is typically seen on ceria supports^{30,31} (Fig. 1c,d and Supplementary Fig. 1). It appears that the initial high temperature treatment has eliminated the sites on which atomically dispersed Pt would reside. Instead we see the formation of 2D rafts as shown in Fig. 1c,d and Supplementary Fig. 1 (labelled with both boxes and arrows), as revealed by the uniform contrast of the domains from centre to edge. The edge-on views confirm the 2D nature of the deposited Pt and the top-down views show the size of the Pt domains to be roughly 1 nm. The extended X-ray absorption fine structure (EXAFS) measurements of this catalyst (Supplementary Fig. 2 and Supplementary Table 2) confirm that this catalyst contains oxidized Pt but has no Pt-Pt neighbours, that is, no Pt metal clusters. This catalyst (which is termed 2Pt/1Pt@CeO₂) contains Pt rafts instead of three-dimensional (3D) metal or oxide clusters.

The CO oxidation reactivity for this $2Pt/1Pt@CeO_2$ catalyst (containing a total of 3 wt.% Pt) is considerably greater than a $3Pt@CeO_2$ prepared via atom trapping (Fig. 2). We found that the reaction rate of $2Pt/1Pt@CeO_2$ catalyst is $103.5 \, \mu mol \, CO \, g_{Pt}^{-1} \, s^{-1}$ at $80 \, ^{\circ}C$ (CO conversion <5%), as opposed to the reaction rate of $10.9 \, \mu mol \, CO \, g_{Pt}^{-1} \, s^{-1}$ on the $3Pt@CeO_2$ single atom catalyst. This is in agreement with a recent study showing that clusters of Pt oxide (for example, Pt_8O_{14} containing Pt–O-Pt sites) are more active in CO oxidation 32 than single atom Pt. We should note that even higher CO oxidation reactivity can be achieved by reducing Pt/CeO $_2$ catalysts 31 , but our focus here is on the oxidized state of the catalyst that is encountered during lean methane oxidation. Under the lean conditions (excess oxygen), the CO oxidation reactivity is reproducible over multiple runs. Low-energy ion scattering (LEIS) (Fig. 2a and Supplementary Table 3), which is surface sensitive, shows

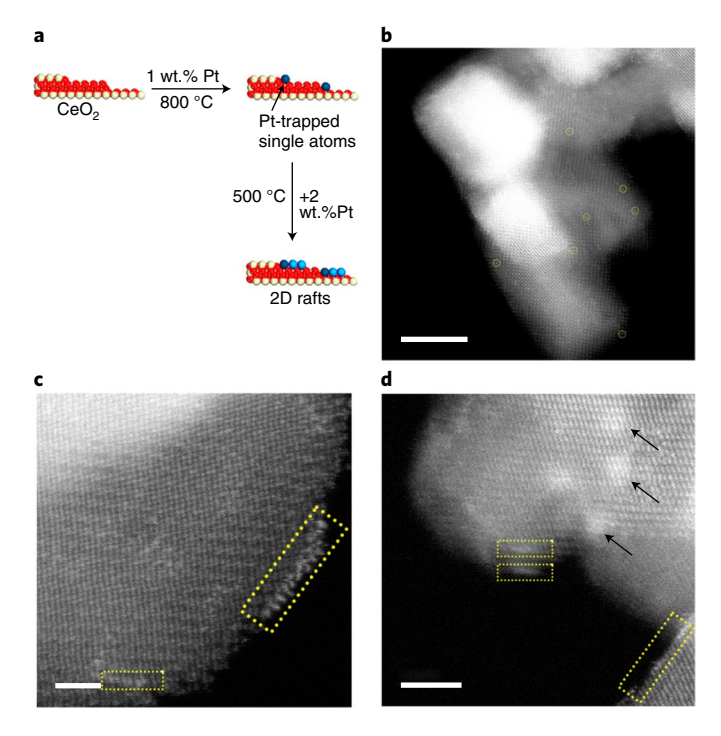


Fig. 1 | Scanning transmission electron microscope images of 2D rafts of Pt on Pt@CeO₂. **a**, Schematic illustration showing the morphologies of Pt catalysts supported on ceria prepared by depositing Pt on a Pt-trapped ceria. The Pt atoms were labelled with different colours for the purpose of emphasizing the two steps in preparation. **b**, AC-STEM image of 1wt.%Pt@CeO₂ prepared by atom trapping showing atomically dispersed Pt indicated by white dots. Scale bar, 5 nm. **c**,**d**, AC-STEM images of the catalyst prepared by depositing 2 wt.% Pt on atom-trapped 1wt.% Pt@CeO₂ showing edge-on views (**c**) and a combination of edge-on and top-down views (**d**) of this sample. Scale bars, 1nm (**c**) and 2 nm (**d**). Edge-on views (**c**,**d**) indicated by rectangles show that Pt forms 2D rafts that are approximately 1.5 nm in diameter as seen in top-down views indicated by arrows in **d**. The uniform contrast of the particles in **d** confirms that these are not three-dimensional nanoparticles, which is a result of the modification of the catalyst support via atom trapping.

that the measured Pt concentration on the 2Pt/1Pt@CeO2 catalyst (1.8 atoms per nm²) exceeds the expected surface concentration (roughly 1.2 atoms per nm²) calculated on the basis of the Pt content and the Brunauer-Emmett-Teller (BET) surface area (Supplementary Table 1). In our previous work on atom-trapped Pt/ CeO₂ we reported the upper limit of Pt surface concentration in single atom catalysts on this same ceria support to be roughly 1 atom per nm² (ref. ³⁰). These results should be put in context with the surface concentration of Ce on the CeO₂ (111) facet that is 7.9 atoms per nm² (ref. ³³) and the Pt surface concentration in an oxidized Pt foil that is 9.0 atoms per nm² (Supplementary Table 3). Therefore, the observed surface concentration for 2D Pt rafts of 1.8 atoms per nm² exceeds that expected from atomically dispersed Pt and is consistent with the presence of Pt rafts on ceria (111) surface facets, with a preferred orientation due to prominent (111) facets leading to more prominent exposure of Pt as seen via aberration-corrected scanning transmission electron microscopy (AC-STEM) (Fig. 1c,d).

These results show that by starting with a catalyst support containing 1 wt.% of strongly bound Pt single atoms, we cause the added 2 wt.% Pt to form 2D rafts. To investigate whether this 2D raft morphology was simply a result of the high temperature treatment of the ceria, we prepared a catalyst support by heating the ceria support to 800 °C (which we term presintered or PS ceria). As shown in Supplementary Fig. 3, heating ceria (800 °C, 10 h) causes a

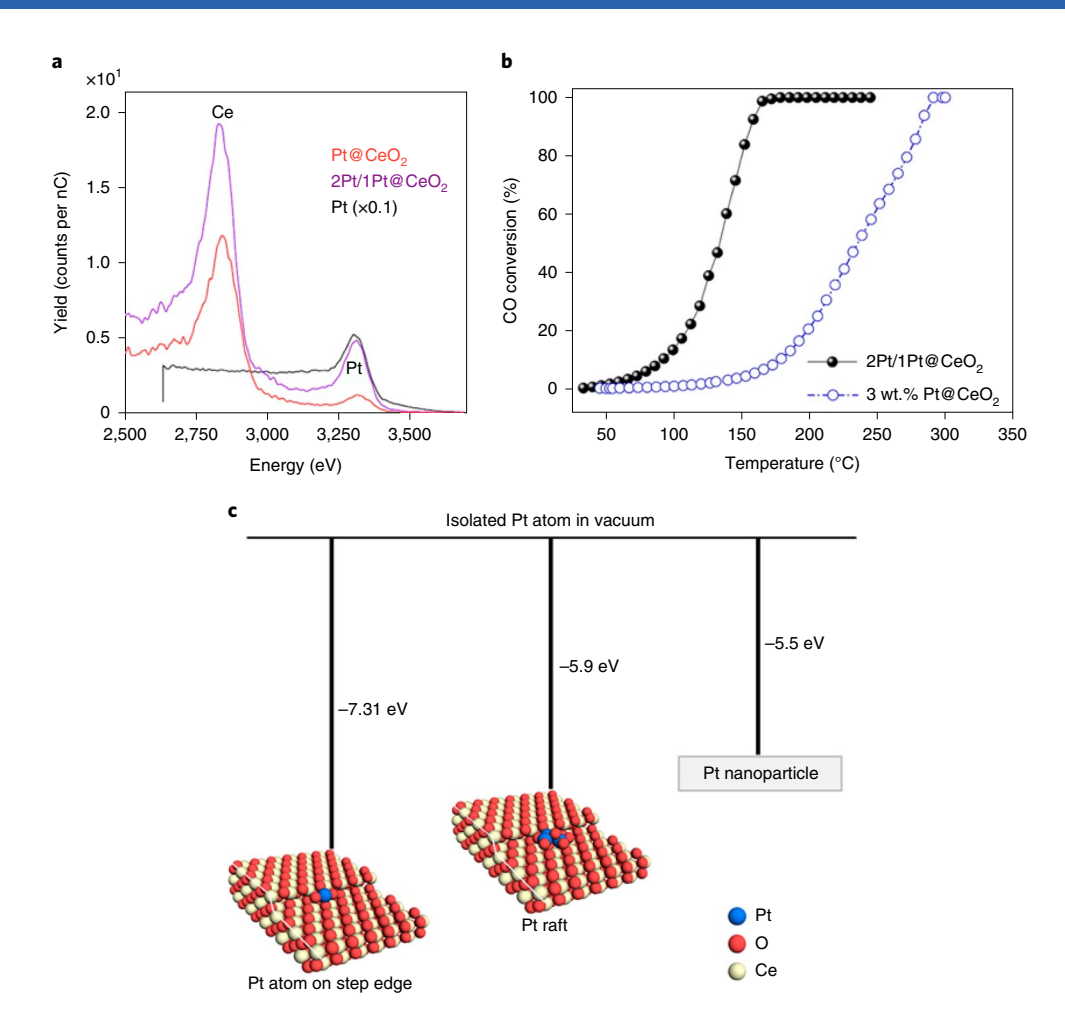


Fig. 2 | CO oxidation reactivity and energetics of Pt 2D rafts deposited on the engineered catalyst support. **a**, LEIS spectra of atomically dispersed 1Pt@ CeO₂ and 2Pt/1Pt@CeO₂, the latter sample contains 2D rafts of Pt as shown in Fig. 1. **b**, The CO oxidation reactivity confirms that the altered morphology of the Pt leads to enhanced CO oxidation reactivity. The 2D Pt rafts (2Pt/1Pt@CeO₂) are more active than the atom-trapped catalyst 3Pt@CeO₂. These two catalysts contain the same amount of Pt, the differences in reactivity can be attributed to different interaction with the support. **c**, The results of DFT computations showing the binding energies of Pt single atoms and a Pt 2D raft joined to the single atom on a CeO₂ step edge, demonstrating the preferential formation of Pt rafts with added Pt to the formation of Pt nanoparticles.

modest loss in surface area of the support (Supplementary Fig. 3d) also leading to well defined ceria (111) surface facets. When we deposited 3 wt.% Pt on the PS ceria and calcined the sample at 500 °C, we observed randomly oriented Pt in the form of 3D nanoparticles (Supplementary Fig. 3c). Therefore, the formation of 2D rafts on 2Pt/1Pt@CeO₂ is very unusual and not simply a result of the high temperature treatment of the ceria support. Using the 1Pt@ CeO₂ as a support modifies the nucleation of the deposited Pt forming 2D rafts instead of 3D nanoparticles that are seen on PS ceria. The facile formation of Pt 2D rafts and the superior reactivity of this catalyst compared to single atom Pt are consistent with the results from our DFT calculations (Supplementary Figs. 4 and 5). Figure 2c presents a summary of the results of DFT computations for the binding energies of Pt single atom on ceria step edges and Pt 2D rafts bound to the single atom located on the CeO₂ step edge compared with the cohesive energy of a Pt nanoparticle, demonstrating the preferential formation of Pt rafts rather than nanoparticles (Supplementary Table 4). In summary, our results show that when the CeO₂ support is modified through the method of atom trapping, the strongly bound Pt single atoms act as templates and nucleation sites, helping the Pt that is subsequently deposited on this support to form 2D rafts, presenting superior CO reactivity compared to the Pt single atom catalyst on CeO₂.

Methane oxidation on Pd deposited on the engineered sup**port.** Inspired by the above observations and results, we deposited Pd (1.09 wt.%) on the engineered ceria support prepared by atom trapping of Pt as described in the previous section. To achieve a 1:1 Pd:Pt molar ratio, we used a catalyst support containing a Pt loading of 2 wt.% prepared via atom trapping (800 °C in air for 10 h) using ceria prepared by decomposition of Ce(NO₃)₃, which we refer to as polyhedral ceria. The performance of this catalyst (1Pd/2Pt@ CeO₂, Pd:Pt atomic ratio of 1:1) was compared with other catalysts on the same ceria support, including the 2Pt@CeO2 used to prepare 1Pd/2Pt@CeO₂, 1Pd/CeO₂ and (1Pd+2Pt)/CeO₂ prepared by impregnation. The reactivity was measured in a fixed bed reactor using a gas mixture that resembles the effluent encountered in the exhaust of lean-burn NGVs (680 ppm CH₄, 14 vol% O₂, 5 vol% CO₂ balanced with N₂ with a total flow of 300 ml min⁻¹). For some of the experiments, we added water vapour (4% and 10% H₂O) to investigate the water tolerance of these catalysts. The light-off curves show that the 1Pd/2Pt@CeO2 catalyst is more active than the oxidized 2Pt@CeO2 and 1Pd/CeO2 catalysts containing the same amount of the corresponding metal atoms under dry methane oxidation conditions (Fig. 3a). The 1Pd/2Pt@CeO2 catalyst also shows improved low-temperature reactivity compared to the reference (1Pd+2Pt)/ CeO₂ catalyst prepared using the same ceria support (twice as high

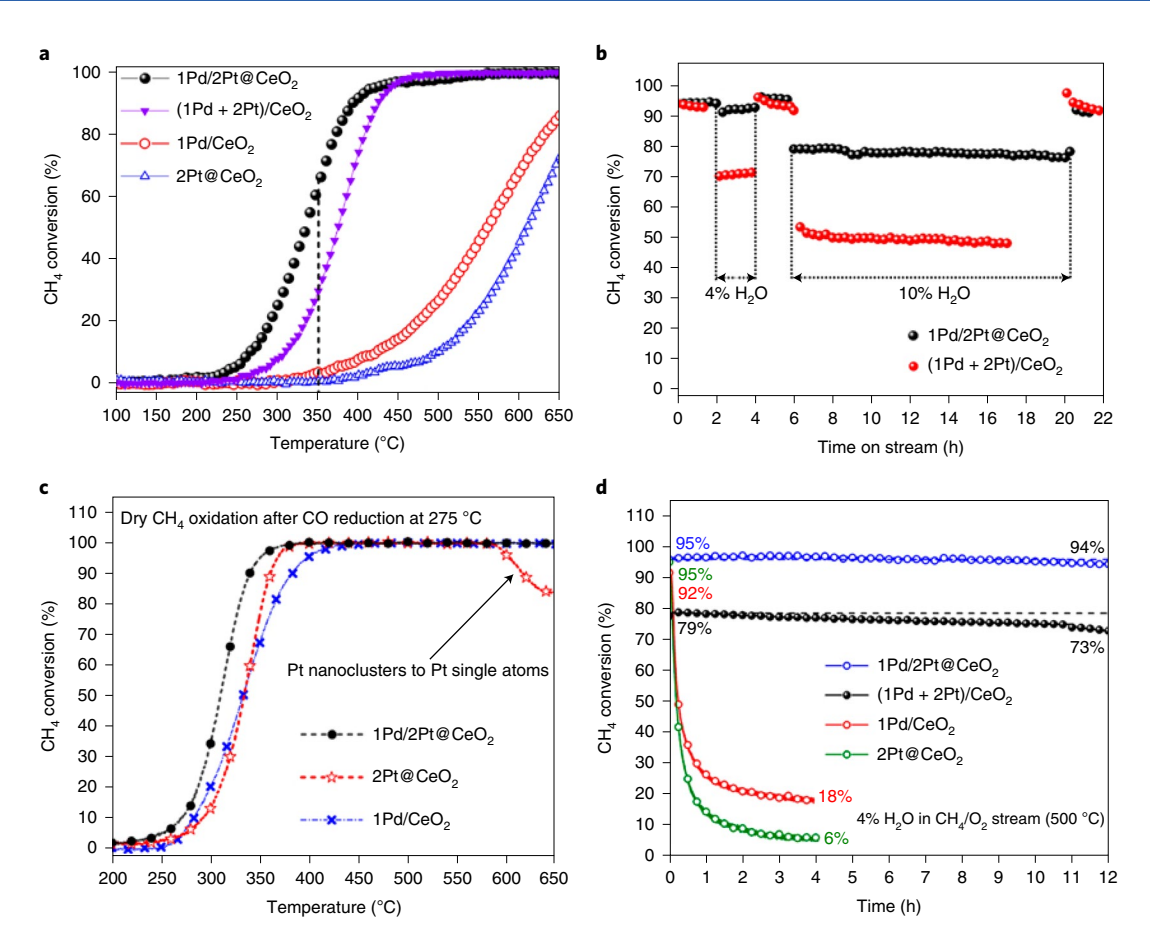


Fig. 3 | Methane oxidation reactivity of Pd-based catalysts with and without added water vapour. a, Light-off curves of CH_4 oxidation under dry conditions over the $1Pd/2Pt@CeO_2$, $(1Pd+2Pt)/CeO_2$, $2Pt@CeO_2$ and $1Pd/CeO_2$ catalysts. b, Time-on-stream measurements for CH_4 oxidation at 500 °C under different steam concentrations over $1Pd/2Pt@CeO_2$ catalysts. c, Light-off curves of CH_4 oxidation under dry conditions over the reduced $1Pd/2Pt@CeO_2$ and $1Pd/CeO_2$ catalysts. d, Comparison of catalyst stability for the as-synthesized $1Pd/2Pt@CeO_2$ and $(1Pd+2Pt)/CeO_2$ catalysts, reduced $2Pt@CeO_2$ and reduced $1Pd/CeO_2$ catalysts in CH_4 oxidation at 500 °C in 4% H_2O showing the excellent water tolerance of $1Pd/2Pt@CeO_2$ (the $Pt@CeO_2$ and Pd/CeO_2 catalysts were prereduced at 275 °C in CO to achieve a comparable initial activity).

at 350 °C). The reference catalyst involved a conventional preparation via impregnation and calcination at 500 °C in air, but without any high temperature (800°C) treatment. It should be mentioned that the 1Pd/2Pt@CeO2 catalyst is stable at higher reaction temperatures and there is no change for the catalyst from 500-650 °C, although the 1Pd/2Pt@CeO2 catalyst was calcined at 500°C and the light-off measurements of catalytic CH₄ combustion were performed up to 650 °C. Indeed, low-temperature methane oxidation is preferred in exhaust catalysis to meet future emission regulations³⁴, especially for lean-burn NGVs where the exhaust temperature is typically below 500-550 °C (ref. 29). We also investigated the reaction rate of the 1Pd/2Pt@CeO₂ and (1Pd+2Pt)/CeO₂ catalysts in kinetic regime by controlling the methane conversion '10%. The 1Pd/2Pt@ CeO₂ catalyst exhibits higher reaction rates with a lower activation energy than that of (1 Pd + 2Pt)/CeO₂ catalyst (Supplementary Fig. 6 and Supplementary Table 5). At 300 °C, the reaction rate of the 1Pd/2Pt@CeO₂ catalyst (3.27 mmol CH₄ mol_{Pd}⁻¹ s⁻¹) is three times higher than that of $(1Pd + 2Pt)/CeO_2$ (0.91 mmol CH₄ mol_{Pd}⁻¹ s⁻¹) under the same reaction conditions.

To test the catalyst stability with and without added water vapour, methane oxidation was carried out at $375-500\,^{\circ}\text{C}$. In the presence of $4\%\text{H}_2\text{O}$, the $1\text{Pd}/2\text{Pt}@\text{CeO}_2$ catalyst is very stable at low reaction temperatures (375 and 450 °C) and there is no observed deactivation during a long TOS (time on stream) run (Supplementary Fig. 7). When the reaction was carried out at $500\,^{\circ}\text{C}$ in dry condition, the

conversion of the catalyst was between 90 and 100% (Fig. 3b,c). Compared to the reactivity of the catalyst under dry methane feed, the methane conversion of the 1Pd/2Pt@CeO2 catalyst presents 3.8% reactivity loss in 4v/v% water and 15.7% reactivity loss in 10 v/v% water, respectively, and the reactivity recovered completely after stopping water vapour flow (Fig. 3b). However, the methane conversion loss of (1 Pd + 2Pt)/CeO₂ catalyst under the presence of 4 and 10% water is 23.2 and 44.3% (Fig. 3b), respectively. This shows the improved water tolerance of 1Pd/2Pt@CeO₂ as compared to (1 Pd + 2Pt)/CeO₂ in methane oxidation (Fig. 3b). Multiple runs of the 1Pd/2Pt@CeO₂ catalyst also demonstrate the reproducibility of the data at both dry and wet conditions (Supplementary Fig. 8a,b). The light-off curves in the presence of varying amounts of water vapour (4 and 10%) for the 1Pd/2Pt@CeO₂ and (1Pd+2Pt)/ CeO₂ catalysts are shown in the Supplementary Fig. 8c,d. The reactivity of both 1Pd/2Pt@CeO2 and (1Pd+2Pt)/CeO2 catalysts was also tested in a kinetically controlled regime where methane conversion was less than 25% and in the presence of 4% water vapour (Supplementary Fig. 8e). It was found that both catalysts were stable but the $1Pd/2Pt@CeO_2$ was more active than the (1Pd+2Pt)/2CeO₂ catalyst, similar to the results observed at high conversions as reported earlier.

While methane oxidation catalysts operate under lean conditions (excess oxygen), we have seen in previous work that reduction of the catalyst forming metallic particles, or periodic pulses under

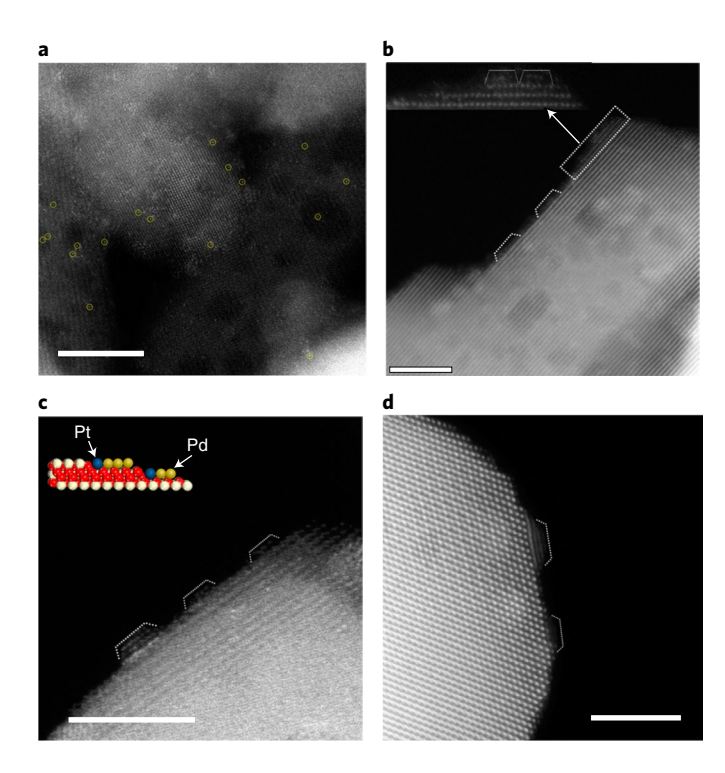


Fig. 4 | AC-STEM images of atom-trapped $2Pt@CeO_2$ and 1Pd deposited on atom-trapped $2Pt@CeO_2$ ($1Pd/2Pt@CeO_2$). **a**, AC-STEM images of $2Pt@CeO_2$ prepared via atom trapping showing single atoms of Pt. **b-d**, AC-STEM image of Pd deposited on the catalyst shown in **a**. Different regions of the sample are imaged in panels **b**, **c** and **d**, and they all show that 2D rafts are visible that look similar to the 2D rafts shown in Fig. 1c. Scale bars, 5 nm.

reducing conditions, lead to enhanced reactivity¹⁷⁻¹⁹. In previous work, we have found that CO reduction at 275°C is sufficient to reduce single atom catalysts and achieve optimal CO oxidation reactivity³¹. Therefore, we tested the performance of these catalysts after CO reduction (Fig. 3c). We see definite improvement in the light-off curve for the bimetallic as well as the monometallic reduced 2Pt@CeO2 and 1Pd/CeO2 catalysts (Fig. 3c), but the bimetallic 1Pd/2Pt@CeO2 catalyst performs better than monometallic Pt or Pd and is stable at high reaction temperatures (>550 °C). At these high conversions, the methane is consumed so the catalyst is being subjected to an oxidizing atmosphere, which shows the improved thermal stability of this catalyst. While the Pd-only catalyst shows similar stable performance under oxidizing conditions (since it forms PdO, which is known to be active at high temperatures), the Pt only catalyst suffers a loss in reactivity. We attribute this loss of activity to the oxidation of the Pt nanoclusters and also possible redispersion to form Pt single atoms under oxidizing conditions at elevated temperature (Fig. 3c).

While the reduced Pd and Pt catalysts show improved reactivity after reduction (Fig. 3c), the performance of these catalysts cannot be sustained during methane oxidation and in the presence of water vapour (Fig. 3d). These catalysts suffer a major loss in reactivity due to oxidation of the metal and poisoning by water vapour. In contrast, the $1Pd/2Pt@CeO_2$ catalysts shows only a slight drop in the long-term run (12h) at $500\,^{\circ}C$ (Fig. 3d). This slight drop (roughly 1%) is probably caused by the large amount of water molecules produced in the reaction at the high conversion of this test. Furthermore, the $(1\,Pd+2Pt)/CeO_2$ catalyst prepared by impregnation shows observed deactivation in the $12\,h$ run in the presence of $4\%\,H_2O$ (decreased from 79 to 73%). These results show that under the conditions of lean methane oxidation, the contribution from

the starting single atom 2Pt@CeO₂ is negligible. Since the bimetallic catalyst 1Pd/2Pt@CeO₂, (1Pd+2Pt)/CeO₂ and the 1Pd/CeO₂ contain similar amounts of Pd, the enhanced performance of the 1Pd/2Pt@CeO₂ catalyst must be attributed to the morphology of the Pd phase presented on the 2Pt@CeO₂ support, which is what we describe next.

The morphology of the 1Pd/2Pt@CeO2 catalyst was studied via AC-STEM. Figure 4a shows that the engineered catalyst support 2Pt@CeO2 contains atomically dispersed Pt species on the ceria support (circles in Fig. 4a), as also seen in both 1Pt@CeO, and 3Pt@ CeO₂ reported in our previous study^{26,30}. After depositing Pd on the 2Pt@CeO₂ material, as shown in Fig. 4b-d, both single atoms and rafts with an average diameter of roughly 0.8 nm are present (Fig. 4b-d and Supplementary Fig. 9). We note that the single atoms seen in these images come from Pt and not Pd, because the contrast of single atom Pd on ceria is not sufficient to make them visible in AC-STEM images (atomic number of Pd is lower than that of Ce, 46 versus 58). Therefore, we can only detect the 2D rafts of Pd rather than Pd single atoms, and since the oxidation state cannot be inferred from this image, we will refer to them as Pd/PdO (PdO_v). The high magnification STEM-EDS mapping (Supplementary Fig. 9b) shows that both Pt and Pd are well dispersed on this catalyst and the homogeneous contrast in a domain indicates that the Pd/PdO domains are not 3D clusters, which would generally show a brighter centre. A schematic view of the morphology of the Pd/PdO on 2Pt@CeO2 is shown in the inset of Fig. 4c. The AC-STEM images (Fig. 4b-d) and the similarity in the image contrast of these Pd/PdO domains to the Pt clusters shown in Fig. 1 allows us to assign these as Pd/PdO 2D rafts that are present on the atomically dispersed 2Pt@CeO₂.

The environment of the Pt and Pd atoms in the PdO, 2D rafts of the 1Pd/2Pt@CeO₂ catalyst was further examined via X-ray absorption spectroscopy (XAS) measurements performed on the calcined samples (Fig. 5). The Pt L₃ edge X-ray absorption near edge structure (XANES) spectrum of 1Pd/2Pt@CeO2 shows that the Pt is oxidized (Fig. 5a), which is similar to the 1Pt@CeO₂ catalyst reported previously³⁵. Likewise, the Pd K edge XANES spectrum of the as-prepared 1Pd/2Pt@CeO2 resembles the bulk references PdO and Pd(OAc)₂. The EXAFS fits for these samples are shown in the Supplementary Information (Supplementary Tables 6-12 and Supplementary Figs. 10–16). The Pt L₃ edge EXAFS has one main peak due to Pt-O scattering, fitting gave a coordination number of 6 ± 0.4 at a bond distance of 1.99 ± 0.008 Å. A Pt-O coordination number of 6 is consistent with platinum in the +4 oxidation state. Previous reports on atom-trapped Pt on CeO₂ gave a Pt-O coordination number of 5, the extra oxygen coordination probably comes from oxygen in the PdO_x rafts as seen in the STEM results³⁰. The interface between the raft structure and the support is not strongly ordered as evidenced by a weak broad doublet peak at 2.8-3.4 Å (phase uncorrected distance) in the Pt EXAFS. The EXAFS at the Pd K edge for 1Pd/2Pt@CeO2 resembles that of bulk PdO with attenuated second and third shell Pd-Pd scattering³⁶. Two models were used to fit the spectrum: a spherical PdO nanoparticle model and a multi-shell PdO model without the shape function constraint. While both models gave equivalent reduced chi squared statistics, the R factor for the multi-shell model was lower. This would be expected if the nanoparticle shape deviated from spherical. The misfit primarily comes from underfitting the second Pd-Pd coordination number. In a disc-shaped particle, a spherical shape function will correctly model the data at distances lower than the shorter of the two characteristic lengths (radius and thickness)³⁷. From the STEM results showing that the rafts are 1-2 atoms thick and on the basis of the lattice parameter of PdO, the spherical model would start to fail past the first Pd-Pd path at 3.02 Å, which is seen in the misfit of the second Pd-Pd path in the spherical model. Indeed, as seen from the Pd K EXAFS spectra (Fig. 5d), the PdO-like structure on 1Pd/2Pt@CeO2 is slightly

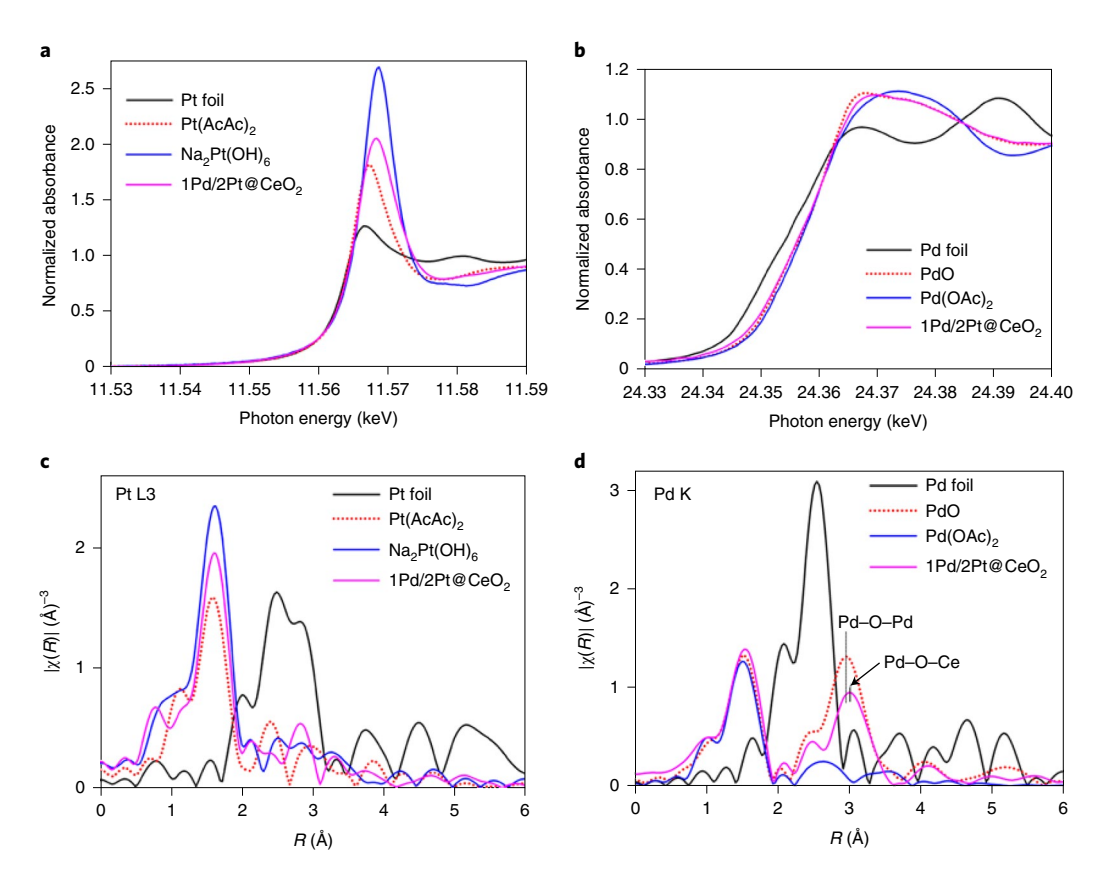


Fig. 5 | XAS spectra of 1Pd/2Pt@CeO₂ sample. a,b, XANES spectra of Pt L₃ (a) and Pd K (b) edges. c,d, EXAFS spectra of the Pt (c) and Pd K (d) edges. The Pt and Pd standard samples were also measured.

different from bulk PdO where the second shell consists of only Pd–Pd scattering. In the catalyst, the second shell includes both Pd–Pd scattering from within the raft and Pd-Ce scattering between the raft and support (Supplementary Fig. 16 and Supplementary Table 12). This agrees well with the observation of STEM results showing the presence of raft-like Pd oxides.

We used surface sensitive X-ray photoelectron spectroscopy (XPS) to reveal the differences in the Pd, Pt and Ce species on the 1Pd/2Pt@CeO2 catalyst compared to the reference (1Pd+2Pt)/ CeO₂ sample prepared by conventional impregnation (Fig. 6 and Supplementary Fig. 17). Reactivity data showed that the reference (1Pd+2Pt)/CeO₂ sample shows lower reactivity than the atom-trapped 1Pd/2Pt@CeO₂ catalyst (Fig. 3a). The Pd 3d binding energy of Pd species on 1Pd/2Pt@CeO₂ is lower than that of the reference (1Pd+2Pt)/CeO₂ (Fig. 6b). This is suggestive of a different form of Pd oxide on the 1Pd/2Pt@CeO2 surface, probably because it is present in the form of a raft, and different from 3D particles of bulk PdO present in the reference sample. The Pt 4f spectrum of 1Pd/2Pt@CeO2 shows peaks at a higher binding energy in comparison to that of the reference (1Pd + 2Pt)/CeO₂ (Fig. 6a), confirming that the Pt species strongly bound to ceria via atom trapping in 1Pd/2Pt@CeO2 are different from Pt that is deposited by impregnation and calcined at 500 °C in air. We performed deconvolution on the Pt 4f, Pd 3d and Ce 3d XPS spectra of the 1Pd/2Pt@CeO₂ and (1 Pd + 2Pt)/CeO₂ catalysts. The Pt 4f XPS spectra show that both Pt2+ and Pt4+ are present on the 1Pd/2Pt@CeO2 and (1Pd+2Pt)/ CeO₂ samples. However, 1Pd/2Pt@CeO₂ presents 38% Pt⁴⁺, as opposed to 8% Pt4+on the (1Pd+2Pt)/CeO₂ sample, meaning more Pt species is strongly trapped via atom trapping on the 1Pd/2Pt@ CeO₂. The deconvolution shows small amount of metallic Pt° (6%) is also present in the (1Pd+2Pt)/CeO₂ sample. The deconvolution

of Pd 3d XPS spectra of the catalysts show that large amount of Pd^{δ +}(δ <2) species (46.8%) are formed on the 1Pd/2Pt@CeO $_2$ catalyst, which is attributed to the presence of PdO $_x$ rafts. In contrast, PdO is the main phase on the reference (1Pd+2Pt)/CeO $_2$ sample. Therefore, the XPS agrees well with the STEM results. The Ce 3d XPS spectra of the catalysts (Supplementary Fig. 17 and Supplementary Table 13) show that the Ce 3 +/Ce 4 + ratio on the 1Pd/2Pt@CeO $_2$ catalyst is higher than that on the (1Pd+2Pt)/CeO $_2$ catalyst (0.27 versus 0.2), suggesting more oxygen vacancies are present on the surface of the 1Pd/2Pt@CeO $_2$ catalyst supported on the engineered support via atom trapping.

The trapping of the Pt is also confirmed by CO-diffuse reflectance infrared Fourier transform spectroscopy (DRIFTS) experiments wherein the 1Pd/2Pt@CeO2 catalyst shows the intense CO band on ionic Pt seen in previous work²⁶ (Supplementary Fig. 18). The Pd in the 2D rafts is mobile and transforms readily from its oxidized state into a reduced state during CO oxidation at 125 °C (Supplementary Fig. 18). This mobility of Pd is consistent with previous studies of Pd single atom catalysts during CO oxidation³⁸. What is unique to the PdO_x structures stabilized by the single atom Pt on the 1Pd/2Pt@CeO₂ catalyst is the enhanced low-temperature reactivity (more than three times higher at 300 °C) for methane oxidation and improved water tolerance, as compared to the reference (1 Pd + 2Pt)/CeO₂ catalyst prepared by conventional impregnation. Indeed, there is a need to develop catalysts that perform methane oxidation at low temperatures. For example, a study of methane oxidation on Pd/Al₂O₃ by in situ DRIFTS concluded that low-temperature activity could be associated with the transformation of 45% Pd atoms at the top of metal Pd to PdO_x species³⁹. More recently, Duan et al. reported the Al₂O₃-decorated Pd/SiO₂ catalysts using atomic layer deposition exhibit active and stable PdO_x

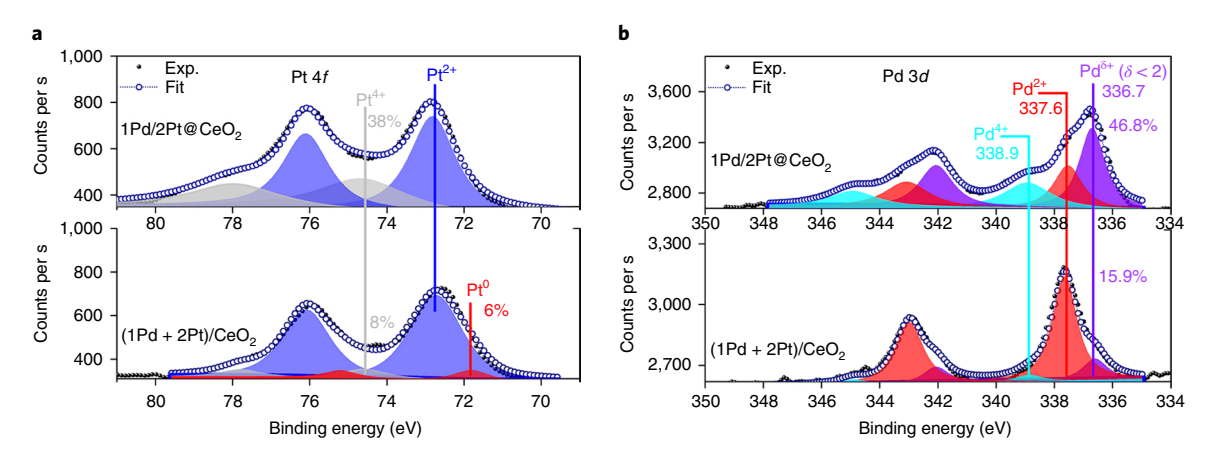


Fig. 6 | XPS spectra of 1Pd/2Pt@CeO_2 and (1Pd + 2Pt)/CeO_2 catalysts. a, Pt 4f XPS spectra showing that the Pt in the catalyst prepared by atom trapping $(1Pd/2Pt@CeO_2)$ is different from Pt deposited by impregnation and calcination $(1Pd + 2Pt/CeO_2)$. **b**, Pd 3d XPS spectra showing a clear difference between the sample prepared by deposition Pd on the atom-trapped Pt $(1Pd/2Pt@CeO_2)$ and the sample prepared by impregnation and calcination of the Pt and Pd precursors $(1Pd + 2Pt)/CeO_2$.

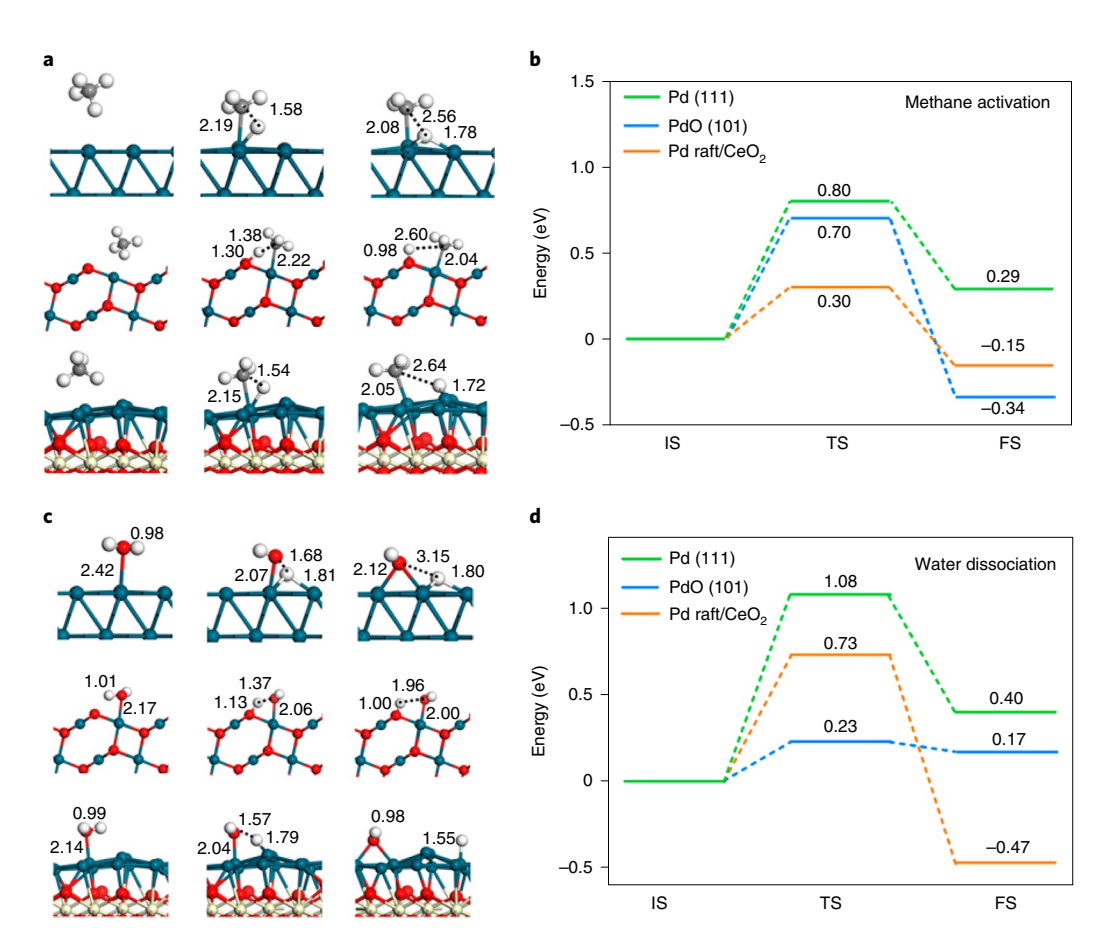


Fig. 7 | DFT simulations of methane oxidation and water dissociation over metal Pd and Pd oxides. a,b, Structures (the initial state (IS), transition state (TS) and final state (FS)) (**a**) and the energy barriers of methane dissociation over the metal Pd (111), PdO (101) and CeO₂ (111) supported 2D PdO raft (**b**) (Supplementary Fig. 19). **c,d**, Structures (IS, TS and FS) (**c**) and the energy barriers of water dissociation over the metal Pd (111), PdO (101) and CeO₂ (111) supported 2D PdO raft (**d**) (0.8 nm). colour scheme: Ce, yellow; Pd, blue; O, red; C, grey and H, white.

and Pd–PdO $_x$ structures to efficiently catalyse methane combustion starting from 200 °C (ref. 22). Later, Yang et al. 40 found that the addition of irreducible oxides in Pd catalyst preserved a suitable active phase of Pd–PdO $_x$ on MgAl $_2$ O $_4$, thus promoting activity. The present work provides an approach to directly prepare PdO $_x$ 2D rafts

that are thermally stable, to improve the low-temperature reactivity in methane oxidation at engine conditions.

On the basis of the above characterization results and the negligible reactivity of the atom-trapped 2Pt@CeO₂ support in methane oxidation, we propose that the reactivity of the Pd deposited

on atom-trapped 2Pt@CeO₂ (1Pd/2Pt@CeO₂) is associated with the 2D PdO_x rafts that were detected via AC-STEM, XPS and EXAFS (Figs. 4-6). These rafts exhibit enhanced reactivity compared to the conventional 2Pt/CeO2 and 1Pd/CeO2 catalysts prepared via impregnation. The enhanced reactivity of 2D PdO_x rafts in methane oxidation is confirmed by DFT calculations (Fig. 7a,b). A lower activation barrier (0.30 eV) for the methane activation is seen on the 2D PdO_x rafts in which an island of single layer Pd atoms bonded to O atoms of CeO2 to form a 2D Pd island model having a size of roughly 0.8 nm (Supplementary Fig. 19), as compared to that (0.80 eV) on metal Pd (111) and that (0.70 eV) on PdO (101). On the other hand, the improved water tolerance of 1Pd/2Pt@CeO, in methane oxidation (10% H₂O vapour) can be explained on the basis of DFT calculation results on the dissociation barrier of water molecule on the catalyst (Fig. 7c,d). The calculation results show that water molecule is easily dissociated to chemisorbed H* and OH* species with a low barrier of 0.23 eV when it is on PdO (101). This suggests that the produced OH* species, which has a large binding energy of $-3.14\,\mathrm{eV}$, could poison the PdO surface sites on the 1Pd/CeO₂ catalyst prepared by impregnation, leading to low activity for methane oxidation. While on 2D PdOx rafts and Pd (111), the barriers for the O-H bond cleavage in water is as high as 0.73 and 1.08 eV, respectively. Therefore, when exposed to steam, the 2D PdO_x raft sites (that is, 1Pd/2Pt@CeO₂ catalyst) are resistant to H₂O poisoning, leading to higher reactivity in methane oxidation. The intermediate behaviours of the PdO_x raft between the metallic (Pd (111)) and oxide (PdO (101)) forms originate from the partial oxidation of Pd by their bonding with substrate oxygens, as shown in Fig. 7.

Conclusions

In this study, we used atom-trapped Pt single atoms to modify and engineer the catalyst support to influence the nature of the deposited metal oxide. In the case of Pt deposited on atom-trapped 1Pt@ CeO₂ (2Pt/1Pt@CeO₂), we found that 2D Pt rafts were formed, the support formed prominent ceria (111) surface facets and the preferred orientation caused a higher surface Pt signal in LEIS. The 2D Pt rafts showed higher reactivity in CO oxidation because of a weaker interaction between the Pt and the engineered support. The catalyst with the strongest interaction, 3Pt@CeO2, had the lowest reactivity for CO oxidation. Using a similar atom trapping approach, we prepared a 1Pd/2Pt@CeO2 catalyst that showed much better reactivity than the conventional 1Pd/CeO2, 2Pt@CeO2 and (1Pd + 2Pt)/CeO₂ catalysts containing the same number of Pd metal atoms when tested for methane oxidation. Analogous to the case of 2Pt/1Pt@CeO₂, aberration-corrected electron microscopy results showed that the 1Pd/2Pt@CeO₂ catalyst presents PdO_x 2D rafts with average size of 0.8 nm as well as the presence of Pt single atoms. Further methane oxidation results under the addition of 4–10 v/v% water vapour show that the 1Pd/2Pt@CeO2 catalyst has improved water tolerance in methane oxidation than conventional 1Pd/CeO₂ and (1Pd+2Pt)/CeO₂ catalysts. The critical difference is the nature of PdO_x phase in the 2D rafts, which is similar to a surface oxide on Pd metal surface. The monolayer Pd oxide on metallic Pd is not stable, since the Pd transforms readily to the PdO phase, which is easily poisoned by water vapour. The superior water tolerance of the 1Pd/2Pt@CeO2 catalyst is due to the presence of Pd oxide in the form of 2D rafts on the engineered support prepared via atom trapping. The performance of this PdO_x phase is very different from that of bulk PdO. The experimental observations are rationalized with model DFT calculations that show differences in the interaction of water vapour with the rafts compared with bulk PdO. This work demonstrates that the approach of atom trapping can be used to engineer a catalyst support leading to improved catalytic performance of the deposited phase. We suggest this approach could be added to the toolkit of catalyst designers to develop improved

catalysts since the nucleation and growth of the deposited phase can be modified by the trapped atoms in the support.

Methods

Catalyst preparation. The initial experiments to investigate the role of atom-trapped Pt were performed with the commercial ceria (Solvay-Rhodia HS 5, also referred to as HSA ceria since it has a higher surface area than the ceria prepared by calcination of $Ce(NO_3)_3$, which was used for the Pd–Pt catalysts). To prepare engineered CeO_2 , tetraamineplatinum nitrate solution was impregnated onto CeO_2 powder by conventional wet impregnation, followed by drying at $120\,^{\circ}\text{C}$ for $12\,\text{h}$. The powder was then calcined at $800\,^{\circ}\text{C}$ for $10\,\text{h}$ in flowing air. The obtained materials were denoted as $1Pt@CeO_2$ and $3Pt@CeO_2$, corresponding to the Pt loadings of 1 and 3 wt.%, respectively. The high temperature treatment causes a drop in BET surface area, from $135\,\text{m}^2\,\text{g}^{-1}$ for the as-received ceria to $60\,\text{m}^2\,\text{g}^{-1}$ for the pure ceria (PS ceria), $78\,\text{m}^2\,\text{g}^{-1}$ for $1Pt@CeO_2$ and $100\,\text{m}^2\,\text{g}^{-1}$ for the $3Pt@CeO_2$ sample. The Pt interacts strongly with the ceria surface, pinning defect sites and slowing the rate of ceria sintering 26,35 .

The nucleation and growth of Pt on PS CeO₂ support (precalcined at 800 °C in air for 10 h) and the 1Pt@CeO₂ (subjected to a similar thermal treatment) helped identify the role of trapped Pt atoms during catalyst preparation. An appropriate amount of tetraamineplatinum nitrate (Pt(NH₃)₄(NO₃)₂) was added to each support followed by drying at 120 °C for 12 h and calcination at 500 °C for 4 h in air. The total Pt loading for each catalyst was 3 wt.% Pt and the samples were denoted as 3 wt.%Pt/PS ceria and 2Pt/1Pt@CeO₂.

For the methane oxidation study, we used ceria powder prepared in the laboratory via decomposition of Ce(NO₃)₃, as described in our previous work²⁶. This ceria powder has a BET surface area of 85 m² g⁻¹ as prepared. To prepare the engineered catalyst support, we used 2 wt.% Pt via impregnation, drying in air, calcination at 500 °C following by ageing in air at 800 °C for 10 h. This catalyst support is denoted as 2Pt@CeO2. Palladium nitrate (1.09 wt.% Pd) was deposited on the 2Pt@CeO2 by wet impregnation, followed by drying at 120 °C for 12 h and calcining at 500 °C for 4h in air. The catalyst was denoted as 1Pd/2Pt@CeO₂. To provide a comparison, we also prepared two reference samples of 1Pd/CeO₂ (1.09 wt.%Pd) and (1Pd+2Pt)/CeO₂ containing the same loading of metal as the 1Pd/2Pt@CeO2. For the reference (1Pd+2Pt)/CeO2 catalyst (BET surface area 64 m² g⁻¹), the palladium(II) nitrate solution was impregnated onto the CeO₂ first, then dried at 120 °C in air for 12 h. After calcination at 500 °C in air for 4h, tetraamineplatinum nitrate (2wt.% Pt) was impregnated onto the material progressively, followed by drying at 120 °C for 12 h in air and calcining at 500 °C for 4h in air. The reference 1Pd/CeO₂ (1.09 wt.%Pd) sample was prepared by impregnating appropriate amount of palladium(II) nitrate solution onto the CeO2. Then, the sample was obtained after drying at 120 °C in air for 12 h and calcining at 500 °C in air for 4h. The morphological properties of this set of catalysts are shown in Supplementary Table 1.

Catalyst characterization. AC-STEM was carried out using a FEI Titan Themis transmission electron microscope equipped with the Gatan K2-IS camera. We also used a JEOL ARM200CF microscope for some of the samples. In each case, the sample powders were deposited on holey carbon films after being dispersed in ethanol. The Pt single atoms on CeO2 can be clearly seen in the AC-STEM dark field images. LEIS was used to quantify the concentration of Pt atoms on the catalyst surface. This technique selectively detects the topmost atoms and was carried out using an IONTOF Qtac100 instrument. The dedicated LEIS instrument was equipped with a double toroidal analyser for the energy analysis of the backscattered ions and the analyser has a large solid angle of acceptance (full 360° azimuth), while the scattering angle is fixed at 145°. In combination with parallel energy detection, this gives a high sensitivity while maintaining the mass resolution. He+ and Ne+ with ion energy 3 and 5 keV and current 5 and 2 nA, respectively, were used to analyse the surface concentration of Pt2+ ions in the catalysts. The area scanned per sample by these two ions was 2×2 mm² and the ion flux used was 1.4×10^{14} ions per cm² and 2.8×10^{13} ions per cm², respectively. The spectra for the Pt reference were analysed within a 1.5 × 1.5 mm² sputter crater over an area of 1×1 mm². The analysis time was adjusted such that the surface damage was the same as for the other spectra. Assuming a sputter coefficient of 0.1 for He and 1 for Ne, this will lead to a surface damage of 1 and 2% at the end of the analysis. XPS was performed using a Kratos Axis Ultra photoelectron spectrometer equipped with a monochromatic Al Ka source operating at 300 W. The base pressure was 2.7×10^{-8} Pa and operating pressure was 2.7 × 10⁻⁷ Pa. Analysis of the XPS spectra was performed using CASA XPS software. X-ray absorption spectroscopy was performed at the Materials Research Collaborative Access Team (MRCAT) bending magnet and insertion device lines at the Advanced Photon Source, Argonne National Laboratory. Measurements at the Pd K edge were performed in transmission mode using a set of three ion chambers that allowed for concurrent measurement of a Pd foil energy reference. Measurements at the Pt edge were performed in fluorescence mode using a Lytle detector with a zinc foil filter used to reduce background fluorescence. At both edges, sample wafers were pressed in a stainless-steel sample holder and measured at room temperature in air. We carried out data analysis using Artemis and Athena in the Demeter software suite41 with phase

and amplitude functions generated by FEFF software using bulk references. At each edge, the amplitude reduction factor (S_0^2) was determined by fitting the first shell scattering of the respective metal foil. The obtained S_0^2 was then fixed in catalyst samples. A spherical nanoparticle shape function was used in the modelling of 1Pd/2Pt@CeO $_2$ at the Pd K edge 42 . Full model and fit details are given in the Supplementary Information.

Catalytic reactivity measurements. CO oxidation was chosen as a probe reaction. The reaction rate measurements were performed using 0.6 cm (1/4 inch) diameter U-tube with 20 mg of sample. The gas flow rates for CO oxidation were the following: CO 1.5 ml min $^{-1}$, O_2 1 ml min $^{-1}$ and He 75 ml min $^{-1}$ and temperature ramp rate was at 2 °C min $^{-1}$. The as-prepared, air-exposed catalyst was loaded into the reactor and temperature was increased to 300 °C under He. Once at 300 °C, a pretreatment with 10% O_2 was performed for 30 min. The gas was then switched to He and the catalyst was cooled to the reaction temperature. Subsequently, CO oxidation kinetic measurements were performed. The total pressure during CO oxidation was 83.3 kPa, the atmospheric pressure in Albuquerque. The products were analysed by an Agilent Micro GC 490.

Catalytic methane (CH₄) combustion for the as-synthesized 1Pd/2Pt@CeO₂ and (1Pd+2Pt)/CeO2 catalysts was performed using a fixed bed flow reactor under industrially relevant conditions. Then 60 mg of catalyst powder was diluted by 600 mg SiC to guarantee isothermal conditions. The catalyst bed was packed between two quartz wool plugs inside a 0.6 cm (1/4 inch) quartz tube. The reaction was performed at atmospheric pressure. The reaction gas consisted of 680 ppm CH₄, 14 vol% O₂ and 5 vol% CO₂ balanced with N₂ with a total flow of $300\,\text{ml}\,\text{min}^{-1}$ (space velocity of $300\,\text{lg}_{\text{cat}}\,\text{h}^{-1}$). Different concentrations of steam (4 and 10% H₂O) were introduced by flowing the reaction gas through a temperature-controlled bubbler. During the measurements, the effluent gas was analysed by an online continuous FTIR MKS 2030 MultiGas Analyser equipped with a LN₂-cooled mercury-cadmium-telluride detector. For light-off measurements, the samples were heated from room temperature to 650 °C with a ramp of 5 °C min⁻¹ in reaction gas. After each light-off test, the system was cooled down in a O₂/N₂ atmosphere. Stability under different dry or wet conditions was also evaluated by time-on-stream measurements at 300-500 °C. The 1Pd/2Pt@ CeO, catalyst is very stable for multiple light-off runs from room temperature to 650 °C. The reactivity and water tolerance of the catalysts at steady state were compared at 500 °C with or without the adding of water vapour because future emission regulations require low-temperature methane oxidation in exhaust catalysis, especially for NGVs where the exhaust temperature is typically below 500-550 °C (refs. 11,43,44). The reaction rate of the $1Pd/2Pt@CeO_2$ and (1Pd+2Pt)/CeO₂ catalysts were also tested in kinetic regime by controlling methane conversion below 10%.

DFT calculations. All spin-polarized DFT calculations were performed using the Vienna Ab initio Simulation Package (VASP)45. The valence electrons were represented by plane waves with a cutoff energy of 400 eV, augmented with the projector-augmented wave pseudopotentials for the core electrons⁴⁶. A Hubbardlike term was added in the so-called DFT + U treatment with $U = 4.5 \,\mathrm{eV}$ applied to the Ce 4f states⁴⁷. For bulk surfaces, the atoms in the top five layers of PdO(101) and the top two layers of Pd (111) were fully relaxed. The reciprocal space was sampled with a k-point mesh of $3 \times 3 \times 1$. For the Pd raft on the engineered Pt@ CeO_2 support via atom trapping, we modelled the slab with a roughly $0.9\times0.8\,\text{nm}$ Pd island on 6 CeO₂ (111) layers, where the Pd island consists of 14 Pd atoms with the average Pd-Pd bond length of 2.69 Å (2.75 Å in Pd bulk) and the average distance between the island and the CeO₂ (111) surface is 1.93 Å. The reciprocal space was sampled with a k-point mesh of $1 \times 1 \times 1$. During geometry optimization, the atoms in the bottom three atomic layers were fixed while others were fully relaxed. The geometric parameters used: Pd-O and Pd-Pd bond lengths in the fixed layers in PdO and Pd models are 2.02 and 2.75 Å, respectively, while for the Pd island model, the Ce-O bond length in fixed layers is 2.29 Å. In these cases, the exchange-correlation potential was treated by the PW91 exchange-correlation functional⁴⁸. A vacuum space larger than 15 Å was set between periodic slabs to avoid the artificial interactions along the z direction. Electronic energy was converged below a threshold of 10⁻⁴ eV, while the force acting on each atom was less than 0.05 eV Å-1. Climbing image nudged elastic band (CI-NEB) approach was used to determine the reaction pathway^{49,50}.

Data availability

The data that support the findings of this study are included in the published article (and its Supplementary Information) or available from the corresponding author on reasonable request. Source data are provided with this paper.

Received: 22 November 2020; Accepted: 27 August 2021; Published online: 18 October 2021

References

 Munnik, P., de Jongh, P. E. & de Jong, K. P. Recent developments in the synthesis of supported catalysts. Chem. Rev. 115, 6687–6718 (2015). Wong, A., Liu, Q., Griffin, S., Nicholls, A. & Regalbuto, J. R. Synthesis of ultrasmall, homogeneously alloyed, bimetallic nanoparticles on silica supports. Science 358, 1427–1430 (2017).

- Bradley, S. A. et al. Behavior of Pt atoms on oxide supports during reduction treatments at elevated temperatures, characterized by aberration corrected stem imaging. *Catal. Lett.* 142, 176–182 (2012).
- Kwak, J. H. et al. Coordinatively unsaturated Al³⁺ centers as binding sites for active catalyst phases of platinum on γ-Al₂O₃. Science 325, 1670–1673 (2009).
- Ding, K. et al. Identification of active sites in CO oxidation and water-gas shift over supported Pt catalysts. Science 350, 189–192 (2015).
- Bo, Z. et al. Strong electrostatic adsorption of Pt onto SiO₂ partially overcoated Al₂O₃—towards single atom catalysts. *J. Chem. Phys.* 151, 214703 (2019).
- Liu, L. & Corma, A. Metal catalysts for heterogeneous catalysis: from single atoms to nanoclusters and nanoparticles. Chem. Rev. 118, 4981–5079 (2018).
- Yao, S. et al. Atomic-layered Au clusters on α-MoC as catalysts for the low-temperature water-gas shift reaction. Science 357, 389–393 (2017).
- Chen, A. et al. Structure of the catalytically active copper–ceria interfacial perimeter. Nat. Catal. 2, 334–341 (2019).
- Lu, J., Elam, J. W. & Stair, P. C. Synthesis and stabilization of supported metal catalysts by atomic layer deposition. Acc. Chem. Res. 46, 1806–1815 (2013).
- Petrov, A. W. et al. Stable complete methane oxidation over palladium based zeolite catalysts. Nat. Commun. 9, 2545 (2018).
- Petrov, A. W., Ferri, D., Kröcher, O. & van Bokhoven, J. A. Design of stable palladium-based zeolite catalysts for complete methane oxidation by postsynthesis zeolite modification. ACS Catal. 9, 2303–2312 (2019).
- Descorme, C., Gélin, P., Lécuyer, C. & Primet, M. Palladium-exchanged MFI-type zeolites in the catalytic reduction of nitrogen monoxide by methane. influence of the Si/Al ratio on the activity and the hydrothermal stability. Appl. Catal. B: Env. 13, 185–195 (1997).
- Li, X., Wang, X., Roy, K., van Bokhoven, J. A. & Artiglia, L. Role of water on the structure of palladium for complete oxidation of methane. ACS Catal. 10, 5783–5792 (2020).
- Huang, W., Goodman, E. D., Losch, P. & Cargnello, M. Deconvoluting transient water effects on the activity of Pd methane combustion catalysts. *Ind. Eng. Chem. Res.* 57, 10261–10268 (2018).
- Zhang, F., Hakanoglu, C., Hinojosa, J. A. & Weaver, J. F. Inhibition of methane adsorption on PdO(101) by water and molecular oxygen. *Surf. Sci.* 617, 249–255 (2013).
- Xiong, H. et al. Design considerations for low-temperature hydrocarbon oxidation reactions on Pd based catalysts. *Appl. Catal. B: Env.* 236, 436–444 (2018).
- Karinshak, K. A., Lott, P., Harold, M. P. & Deutschmann, O. In situ activation of bimetallic Pd-Pt methane oxidation catalysts. *Chem. Cat. Chem.* 12, 3712–3720 (2020).
- 19. Lott, P., Dolcet, P., Casapu, M., Grunwaldt, J.-D. & Deutschmann, O. The effect of prereduction on the performance of Pd/Al₂O₃ and Pd/CeO₂ catalysts during methane oxidation. *Ind. Eng. Chem. Res.* **58**, 12561–12570 (2019).
- Hellman, A. et al. The active phase of palladium during methane oxidation. J. Phys. Chem. Lett. 3, 678–682 (2012).
- Martin, N. M. et al. Intrinsic ligand effect governing the catalytic activity of Pd oxide thin films. ACS Catal. 4, 3330–3334 (2014).
- 22. Duan, H. et al. Pentacoordinated Al^{3+} -stabilized active Pd structures on Al_2O_3 -coated palladium catalysts for methane combustion. *Angew. Chem. Int. Ed.* **58**, 12043–12048 (2019).
- Graham, G. W. et al. Effect of alloy composition on dispersion stability and catalytic activity for NO oxidation over alumina-supported Pt-Pd catalysts. Catal. Lett. 116, 1–8 (2007).
- 24. Yashnik, S. A., Chesalov, Y. A., Ishchenko, A. V., Kaichev, V. V. & Ismagilov, Z. R. Effect of Pt addition on sulfur dioxide and water vapor tolerance of Pd-Mn-hexaaluminate catalysts for high-temperature oxidation of methane. Appl. Catal. B: Env. 204, 89–106 (2017).
- Datye, A. & Wang, Y. Atom trapping: a novel approach to generate thermally stable and regenerable single-atom catalysts. Nat. Sci. Rev. 5, 630–632 (2018).
- Jones, J. et al. Thermally stable single-atom platinum-on-ceria catalysts via atom trapping. Science 353, 150–154 (2016).
- 27. Wei, S. et al. Direct observation of noble metal nanoparticles transforming to thermally stable single atoms. *Nat. Nanotechnol.* **13**, 856–861 (2018).
- Goodman, E. D. et al. Catalyst deactivation via decomposition into single atoms and the role of metal loading. Nat. Catal. 2, 748–755 (2019).
- Jiang, D., Khivantsev, K. & Wang, Y. Low-temperature methane oxidation for efficient emission control in natural gas vehicles: Pd and beyond. ACS Catal. 10. 14304–14314 (2020).
- Kunwar, D. et al. Stabilizing high metal loadings of thermally stable platinum single atoms on an industrial catalyst support. ACS Catal. 9, 3978–3990 (2019)
- Pereira-Hernández, X. I. et al. Tuning Pt-CeO₂ interactions by high-temperature vapor-phase synthesis for improved reducibility of lattice oxygen. *Nat. Commun.* 10, 1358 (2019).

- Wang, H. et al. Surpassing the single-atom catalytic activity limit through paired Pt-O-Pt ensemble built from isolated Pt1 atoms. *Nat. Commun.* 10, 3808 (2019).
- Dvořák, F. et al. Creating single-atom Pt-ceria catalysts by surface step decoration. Nat. Commun. 7, 10801 (2016).
- 34. Farrauto, R. J. Low-temperature oxidation of methane. *Science* 337, 659–660 (2012).
- 35. Nie, L. et al. Activation of surface lattice oxygen in single-atom Pt/CeO₂ for low-temperature CO oxidation. *Science* **358**, 1419–1423 (2017).
- Bugaev, A. L. et al. In situ formation of surface and bulk oxides in small palladium nanoparticles. *Chem. Commun.* 56, 13097–13100 (2020)
- 37. Glatter, O. The interpretation of real-space information from small-angle scattering experiments. *J. Appl. Crystallogr.* **12**, 166–175 (1979).
- 38. Spezzati, G. et al. Atomically dispersed Pd-O species on CeO₂ (111) as highly active sites for low-temperature CO oxidation. *ACS Catal.* 7, 6887–6891 (2017).
- Xu, J. et al. Operando and kinetic study of low-temperature, lean-burn methane combustion over a Pd/γ-Al₂O₃ catalyst. ACS Catal. 2, 261–269 (2012)
- Yang, J. et al. A hydrothermally stable irreducible oxide-modified Pd/MgAl₂O₄ catalyst for methane combustion. *Angew. Chem. Int. Ed.* 59, 18522–18526 (2020).
- Ravel, B. & Newville, M. ATHENA, ARTEMIS, HEPHAESTUS: data analysis for X-ray absorption spectroscopy using IFEFFIT. J. Synchrotron Radiat. 12, 537–541 (2005).
- Calvin, S. et al. Determination of crystallite size in a magnetic nanocomposite using extended X-ray absorption fine structure. *J. Appl. Phys.* 94, 778–783 (2003).
- Lampert, J. K., Kazi, M. S. & Farrauto, R. J. Palladium catalyst performance for methane emissions abatement from lean burn natural gas vehicles. *Appl. Catal. B: Env.* 14, 211–223 (1997).
- Gélin, P. & Primet, M. Complete oxidation of methane at low temperature over noble metal based catalysts: a review. Appl. Catal. B: Env. 39, 1–37 (2002).
- Kresse, G. & Furthmüller, J. Efficient iterative schemes for ab initio total-energy calculations using a plane-wave basis set. *Phys. Rev. B* 54, 11169–11186 (1996).
- Kresse, G. & Joubert, D. From ultrasoft pseudopotentials to the projector augmented-wave method. *Phys. Rev. B* 59, 1758–1775 (1999).
- Huang, M. & Fabris, S. CO adsorption and oxidation on ceria surfaces from DFT+U calculations. *J. Phys. Chem. C* 112, 8643–8648 (2008).
- Perdew, J. P. et al. Atoms, molecules, solids, and surfaces: applications of the generalized gradient approximation for exchange and correlation. *Phys. Rev. B* 46, 6671–6687 (1992).
- 49. Henkelman, G., Uberuaga, B. P., Jónsson, H. & Climbing, A. Image nudged elastic band method for finding saddle points and minimum energy paths. *J. Chem. Phys.* **113**, 9901–9904 (2000).
- Henkelman, G. & Jónsson, H. Improved tangent estimate in the nudged elastic band method for finding minimum energy paths and saddle points. J. Chem. Phys. 113, 9978–9985 (2000).

Acknowledgements

The catalyst synthesis and characterization via transmission electron microscopy (TEM) and DRIFTS was partly supported by DOE/BES Catalysis Science program,

grant no. DE-FG02-05ER15712. Reactivity measurements were supported by the US Department of Energy (DOE) Office of Energy Efficiency and Renewable Energy under the Advanced Manufacturing Office, award number DE-LC 000L059 and from the Vehicle Technologies Office. H.X. acknowledges support from the National High-Level Young Talents programme and National Natural Science Foundation of China (grant nos. 22072118 and 2212100020). The computational work on catalysis was supported by the National Natural Science Foundation of China (grant nos. 21673040 and 21973013) and Air Force Office of Scientific Research (grant no. FA9550-18-1-0413). S.S.C. acknowledges support from the Center for Integrated Nanotechnologies (CINT), a user facility operated for the US DOE Office of Science where some of the characterization was performed. J.H. thanks National Natural Science Foundation of China (grant nos. 51772262, U20A20336 and 21935009), Natural Science Foundation of Hebei Province (grant no. B2020203037) and the Hunan Innovation Team (grant no. 2018RS3091) for financial support of this research. The characterization via XAS was supported by the National Science Foundation under Cooperative Agreement no. EEC-1647722 (CISTAR). Use of the Advanced Photon Source was supported by the US DOE Office of Basic Energy Sciences under contract no. DE-AC02-06CH11357. MRCAT operations, beamline 10-BM and 10-ID, are supported by the DOE and the MRCAT member institutions. We thank A. Genc, H. Pham and F. Shi for assistance with the TEM measurements that were performed, in part, at Thermo Fisher and at the University of Illinois at Chicago, Research Resources Center, Electron Microscopy Core. K.L. and S.S.C. acknowledge support from Sandia National Laboratories, a multi-mission laboratory managed and operated by National Technology and Engineering Solutions of Sandia, LLC, a wholly owned subsidiary of Honeywell International, Inc., for the US DOE's National Nuclear Security Administration under contract no. DE-NA0003525. This paper describes objective technical results and analysis. Any subjective views or opinions that might be expressed in the document do not necessarily represent the views of the US DOE or the United States Government.

Author contributions

S.S.C., H.X., Y.W., H.G. and A.K.D. conceived and planned the research. H.X., D.K., D.J. and H.L. synthesized the catalysts and performed catalyst characterization. DFT computations and analysis were performed by Q.W., S.L., H.G. and K.L. LEIS measurements were done by H.H.B. and R.V. H.X., D.K., C.D., J.H. and G.C. performed the TEM measurements. C.E.G.-V. and X.I.P.-H. did the DRIFTS measurements. S.C.P. and J.T.M. performed the XAS measurements. H.L. and D.J. measured the reactivity. H.X., H.G., Y.W. and A.K.D. wrote the paper. All authors discussed the results and commented on the paper.

Competing interests

The authors declare no competing interests.

Additional information

Supplementary information The online version contains supplementary material available at https://doi.org/10.1038/s41929-021-00680-4.

Correspondence and requests for materials should be addressed to Haifeng Xiong, Hua Guo, Yong Wang or Abhaya K. Datye.

Peer review information *Nature Catalysis* thanks Hyunjoo Lee and the other, anonymous, reviewer(s) for their contribution to the peer review of this work.

Reprints and permissions information is available at www.nature.com/reprints.

Publisher's note Springer Nature remains neutral with regard to jurisdictional claims in published maps and institutional affiliations.

© The Author(s), under exclusive licence to Springer Nature Limited 2021